

Topological properties of spin block magnetic ladders in proximity of a superconductor: application to BaFe_2S_3

Shivam Yadav,^{1,*} Pascal Simon,^{2,†} and Andrzej Ptak^{1,‡}

¹*Institute of Nuclear Physics, Polish Academy of Sciences,
ul. E. Radzikowskiego 152, PL-31342 Kraków, Poland*

²*Université Paris-Saclay, Centre National de la Recherche Scientifique,
Laboratoire de Physique des Solides, 91405 Orsay, France*

(Dated: February 10, 2026)

Monoatomic chains with magnetic order in proximity of a s-wave superconductor can host Majorana edge modes. In this paper, we extend this idea to more complex spin-block chains such as the BaFe_2S_3 magnetic material that has a spin-ladder like structure. We investigate the topological phase diagram of such a system as function of the system parameters. We show that the coupling between chains within the ladder leads to the topological phase with a winding number larger than the sum of two single magnetic chains. Furthermore, strong coupling between chains leads to fractal-like substructure in the topological phase diagram. By investigating the real space properties of such a system and particularly its edge modes, we find that the system spectrum contains several in-gap states that we analyze in detail.

I. INTRODUCTION

The possibility to realize Majorana quasiparticles in spinless fermion chain [1] initiated a period of intensive studies of topological states. Recently, several experimental setups have been proposed for the realization of the Majorana edge modes [2–4]. One of them being a magnetic chain proximitized by a s-wave superconductor [5–13]. The experimental advances have facilitated building magnetic chains using Fe atoms [14–19] or Co atoms [16] by depositing them on a superconducting surface (like lead). However, in such case the topological phase tends to strongly depend on the system parameters [20].

The topological phase can be induced by the magnetic field in the system containing spin-orbit coupling and superconductivity [21–23]. For example, such effect were discussed in the context of Majorana edge modes in semiconducting nanowires with a strong spin-orbit coupling proximized by a superconductor [24–26]. In such situation, the increase in the magnetic Zeeman field, leads to closing of the trivial superconducting gap, and a reopening of a “new” topological gap. The effect of the external Zeeman field can be mimicked by some intrinsic magnetic order realized within the magnetic chain, which in simplest case has ferromagnetic (FM) order. Nevertheless, the realization of the topological phase is not limited to ferromagnetic chains, but also can be realized in the presence of antiferromagnetic (AFM) order [27, 28]. Indeed, recent progress in experimental techniques allow assembly of a magnetic chain by *atom-by-atom* engineering on top of a superconducting substrate [19]. The magnetic order realized within the ad-atom chain can be controlled

e.g. by the relative position with respect to the surface atoms [29–32]. In such case, the topological phase depends strongly on the length of the chain [32, 33]. In most cases, non-collinear magnetic order can support realization of the topological phase as it mimics the effect of a spin-orbit coupling and the Zeeman field [5–13].

In this manuscript, we focus on the BaFe_2Ch_3 ($\text{Ch}=\text{S}, \text{Se}$) compounds [34]. The crystal structure consists of double chains of FeSe_4 edge connected tetrahedra intercalated with barium (Fig. 1). At room temperature, BaFeSe_3 exhibits multiferroic behavior [35–37] and short range magnetic order [38, 39]. External hydrostatic pressure leads to several structural phase transition in both compounds [40–45]. Moreover, the application of pressure (between 10 and 15 GPa) can lead to emergence of a superconducting phase [46, 47]. Finally, one of the most intriguing property is the realization of a block spin magnetic order [48–50], driven by electronic correlation [51–53]. In practice, the BaFe_2Fe_3 is a selective orbital Mott insulator [54, 55]. The long range magnetic order is realized below $T_N \sim 120$ K for BaFe_2S_2 [56], and similarly below $T_N \sim 140$ K for BaFe_2Se_3 [57]. Additionally, the

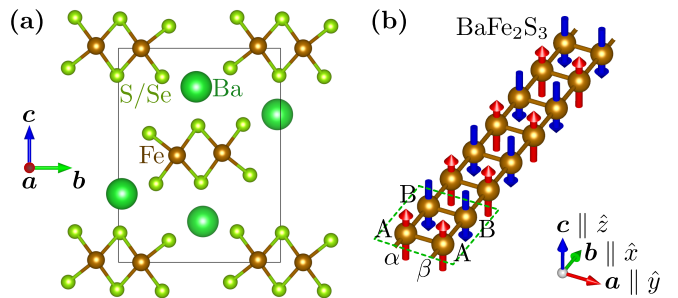


FIG. 1. (a) Crystal structure of BaFe_2Ch_3 ($\text{Ch}=\text{S}, \text{Se}$) with Pnma symmetry. (b) The iron ladder can realize canonical $(\pi, 0)$ AFM-like order in BaFe_2S_3 . Thus the magnetic unit cell contain two pairs of sites.

* e-mail: shivam.yadav@ifj.edu.pl

† e-mail: pascal.simon@universite-paris-saclay.fr

‡ e-mail: aptok@mmj.pl

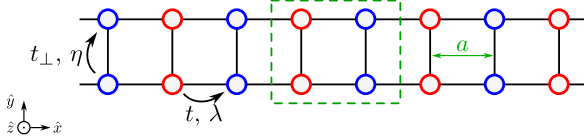


FIG. 2. Schematic model of the investigated ladder mode with spin block order. We assume the spin-conserving electron hopping along chains ($-t$) and between chains ($-t_{\perp}$). Similarly the spin-orbit coupling is assumed along chains (λ) and between chains (η). Lattice constant is the distance between neighbouring sites along x , is taken as $a = 1$. Magnetic sublattices are present by blue and green sites, while the magnetic unit cell is marked by green dashed rectangle.

magnetic order can be modified by the external hydrostatic pressure [44, 45, 58].

The magnetic order realized in BaFe_2S_3 and BaFe_2Se_3 correspond to the canonical $(\pi, 0)$ AFM-like order [see Fig. 1(b)]. The iron ladder exhibit FM coupling between the magnetic moments along the rungs of the ladder. On the opposite, magnetic moments exhibit AFM coupling along the chains of the ladder. For BaFe_2S_3 the magnetic moments changes orientation site-by-site [Fig. 1(b)], while in the BaFe_2Se_3 case, they form a spin block with opposite magnetic moments.

Naturally, the presence of both a FM and AFM-like order raises the question whether topological phases could be realized in such structures when proximitized by a superconductor. This is the question we answer in this manuscript. A previous theoretical investigation of the AFM chain in proximity of a superconductor shows a rich topological phase diagram [28].

In the case of a AFM chain, additional topological regions can be realized in the phase diagram, which in some

situations result in emergence of topological superconducting phases in extremely small magnetic field. Additionally, the topological phase can be found when the Fermi level is not located around some band-edge any longer. In our study, we specifically focus on the ladder with AFM-like order realized e.g. in BaFe_2S_3 [as presented on Fig. 1(b)] but it can be extended to the BaFe_2Se_3 case which exhibits a similar phenomenology.

The paper is organized as follows. In Sec. II, we first present our theoretical model describing a spin-block magnetic ladder and techniques used to study the topological phases. Next, in Sec. III we present and discuss our numerical results aiming at characterizing the various topological phases from a bulk or edge perspective. Finally, we present our main conclusion of the work in Sec. V.

II. MODEL AND TECHNIQUES

In our study we consider the magnetic ladder with AFM-like magnetic order, presented in Fig. 1(b). Such structure is formed by two chains (denoted α and β), while the magnetic unit cell contains two pairs of sites with opposite magnetic moment (with spin \uparrow and \downarrow , called site A and B , respectively). Additionally, we assume that the chains are in xy plane along the \hat{x} direction, while magnetic moments are located along \hat{z} . Thus, the hopping of electrons between sites is realized along the chains (in the \hat{x} direction), and between the chains (in the \hat{y} direction) (Fig. 2). The system can be described by the Hamiltonian:

$$H = H_0 + H_{AFM} + H_{SC}. \quad (1)$$

First term H_0 denotes the free electrons in the ladder:

$$\begin{aligned} H_0 = & -t \sum_{i,w,\sigma} \left[c_{iAw\sigma}^\dagger c_{iBw\sigma} + c_{iBw\sigma}^\dagger c_{i+1Aw\sigma} + h.c. \right] - t_{\perp} \sum_{i,s,\sigma} \left[c_{is\alpha\sigma}^\dagger c_{is\beta\sigma} + h.c. \right] \\ & - \sum_{i,s,w,\sigma} (\mu + \sigma h) c_{isw\sigma}^\dagger c_{isw\sigma} \\ & - i\lambda \sum_{iw\sigma\sigma'} \left(c_{iAw\sigma}^\dagger \sigma_{\sigma,\sigma'}^y c_{iBw\sigma'} + c_{iBw\sigma}^\dagger \sigma_{\sigma,\sigma'}^y c_{i+1Aw\sigma'} + h.c. \right) \\ & - i\eta \sum_{is\sigma\sigma'} \left(c_{is\alpha\sigma}^\dagger \sigma_{\sigma\sigma'}^x c_{is\beta\sigma'} + h.c. \right). \end{aligned} \quad (2)$$

Here, $c_{isw\sigma}$ ($c_{isw\sigma}^\dagger$) denotes the annihilation (creation) operator of an electron with spin σ in the $s = A, B$ sublattice of the $w = \alpha, \beta$ chain in the i^{th} unit cell. The notation $h.c.$ stands for hermitian conjugate. μ and h denote the chemical potential and external magnetic field, respectively. The intra-chain and inter-chain hopping matrix elements are described by hopping integrals t and t_{\perp} , respectively. In what follows, t will be used as the energy unit. Similarly, the Rashba-like spin-orbit coupling (SOC) along the \hat{x} and \hat{y} direction is described by the λ and η parameters, respectively. The separate value of the hoppings and Rashba SOCs along and between the chains allows us to explore the large parameter space of the system and to navigate from two weakly coupled chains to a regime where the chains are strongly coupled.

The second term describes the magnetic order:

$$H_{AFM} = -m_0 \sum_{i w \sigma} \sigma (c_{iAw\sigma}^\dagger c_{iAw\sigma} - c_{iBw\sigma}^\dagger c_{iBw\sigma}). \quad (3)$$

Here, m_0 is proportional to the amplitude of the magnetic moment. The magnetic order naturally introduces two non-equivalent sublattices A and B with opposite magnetic moments. Finally, H_{SC} describes the super-

conducting state induced within the ladder due to the proximity effect with an ordinary s-type superconductor. The pairing term reads:

$$H_{SC} = \Delta \sum_{isw} (c_{isw\uparrow}^\dagger c_{isw\downarrow} + c_{isw\downarrow} c_{isw\uparrow}), \quad (4)$$

where Δ is taken real and corresponds to the amplitude of the proximity induced pairing term.

Assuming periodic boundary conditions, we can write the Hamiltonian in momentum space using the following Fourier transform for the operators:

$$c_{isw\sigma}^\dagger = \frac{1}{\sqrt{N}} \sum_k \exp(-i\mathbf{k} \cdot \mathbf{R}_{is}) c_{ksw\sigma}^\dagger, \quad \text{and} \quad c_{isw\sigma} = \frac{1}{\sqrt{N}} \sum_k \exp(i\mathbf{k} \cdot \mathbf{R}_{is}) c_{ksw\sigma}, \quad (5)$$

where \mathbf{R}_{is} denote position of s th sublattice site (A or B) in i th unit cell, i.e. $\mathbf{R}_{is} = [2i\delta_{sA} + (2i+1)\delta_{sB}]\hat{x}$. Here, $c_{ksw\sigma}$ ($c_{ksw\sigma}^\dagger$) denotes the annihilation (creation) operator of an electron with momentum k in the s magnetic sublattice of the w chain, while N denotes the number of unit cells. As discussed earlier the magnetic unit cell has four sites (one pair of sites per chain), which enforces the Brillouin zone (BZ) to fold on itself hence $k \in [-\pi/2, \pi/2]$. In momentum space, appropriate terms of the Hamiltonian can be rewritten as:

$$\begin{aligned} H_0 &= \sum_{k w \sigma} \mathcal{E}_k (c_{kAw\sigma}^\dagger c_{kBw\sigma} + \text{H.c.}) - \sum_{k s \sigma} t_\perp (c_{ks\alpha\sigma}^\dagger c_{ks\beta\sigma} + \text{H.c.}) - \sum_{k s w \sigma} (\mu + \sigma h) c_{ksw\sigma}^\dagger c_{ksw\sigma} \\ &+ \sum_{k w \sigma \sigma'} i \mathcal{L}_k c_{kAw\sigma}^\dagger \sigma_{\sigma\sigma'}^y c_{kBw\sigma'} + \text{H.c.} - \sum_{\substack{k s w \\ w' \sigma \sigma'}} i \eta c_{ksw\sigma}^\dagger \sigma_{\sigma\sigma'}^x c_{ksw'\sigma'} + \text{H.c.}, \end{aligned} \quad (6)$$

$$H_{AFM} = -m_0 \sum_{k w \sigma} \sigma (c_{kAw\sigma}^\dagger c_{kAw\sigma} - c_{kBw\sigma}^\dagger c_{kBw\sigma}), \quad (7)$$

$$H_{SC} = \Delta \sum_{k s w} (c_{ksw\uparrow}^\dagger c_{-ksw\downarrow} + c_{-ksw\downarrow} c_{ksw\uparrow}). \quad (8)$$

Here, $\mathcal{E}_k = -2t \cos k$, and $\mathcal{L}_k = -2i \sin k$. As we can see, the presented model can also be interpreted as two-orbital (α and β wires) system with hybridization t_\perp and η between orbitals at the same (A and B) sites.

We wish to write the Hamiltonian in the basis of tensor product of four Pauli matrices. We therefore introduce τ which acts on particle hole subspace, ρ for the sublattice subspace, ν representing the chain subspace, and σ which acts in the spin subspace. Using such a representation the

Hamiltonian reads:

$$H = \sum_k \psi_k^\dagger \mathbb{H}_k \psi_k, \quad (9)$$

where \mathbb{H}_k is the Hamiltonian in the matrix form for momentum k , while ψ_k^\dagger is the Nambu vector for such a representation is given by:

$$\begin{aligned} \psi_k^\dagger = & \\ & \left(c_{kA\alpha\uparrow}^\dagger c_{kA\alpha\downarrow}^\dagger c_{kA\beta\uparrow}^\dagger c_{kA\beta\downarrow}^\dagger c_{kB\alpha\uparrow}^\dagger c_{kB\alpha\downarrow}^\dagger c_{kB\beta\uparrow}^\dagger c_{kB\beta\downarrow}^\dagger c_{-kA\alpha\uparrow} c_{-kA\alpha\downarrow} c_{-kA\beta\uparrow} c_{-kA\beta\downarrow} c_{-kB\alpha\uparrow} c_{-kB\alpha\downarrow} c_{-kB\beta\uparrow} c_{-kB\beta\downarrow} \right) \end{aligned} \quad (10)$$

The Hamiltonian in matrix form can be represented as:

$$\mathbb{H}_k = \mathcal{E}_k \tau^3 \rho^1 \nu^0 \sigma^0 - t_\perp \tau^3 \rho^0 \nu^1 \sigma^0 - \mu \tau^3 \rho^0 \nu^0 \sigma^0 - h \tau^3 \rho^0 \nu^0 \sigma^3 + i \mathcal{L}_k \tau^3 \rho^1 \nu^0 \sigma^2 + \eta \tau^3 \rho^0 \nu^2 \sigma^1 - \Delta \tau^2 \rho^0 \nu^0 \sigma^2 - m_0 \tau^3 \rho^3 \nu^0 \sigma^3, \quad (11)$$

the superscript labels which ranges from 0 to 3 for all subspaces represent the identity, x , y , and z Pauli matrices respectively in their respective subspaces.

Similar to the previous study [59], the topological in-

properties can be studied using the \mathbb{Z} topological in-

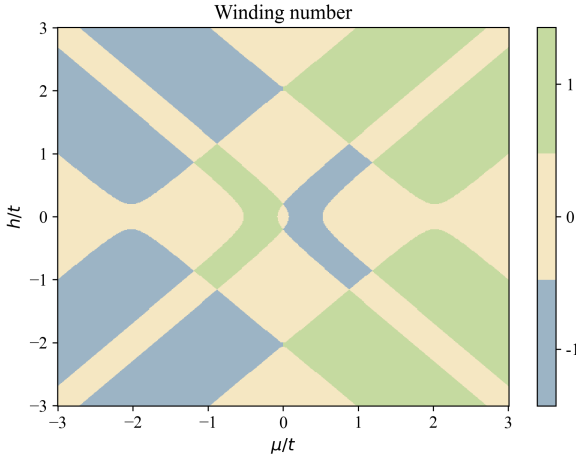


FIG. 3. The topological phase diagram of the one dimensional AFM chain ($t_{\perp} = \eta = 0$). Results obtained for $m_0/t = 0.3$, $\Delta/t = 0.2$, and $\lambda/t = 0.15$, correspond to the study presented in Ref. [28].

variant. In the case of chain-like system the winding number is the corresponding topological invariant, and can be introduced by transforming the Hamiltonian into a block form with a unitary transformation, $\mathcal{U} = \exp(i\frac{\pi}{4}\tau^3)\rho^0\nu^0\sigma^0$. This morphs the Hamiltonian into the following block off diagonal form [59]:

$$\mathbb{H}_k = \begin{pmatrix} 0 & \mathcal{A}(k) \\ \mathcal{A}^{\dagger}(-k) & 0 \end{pmatrix}. \quad (12)$$

The winding number now reads as

$$\mathcal{W} = \frac{1}{2\pi i} \int_{k=-\frac{\pi}{2}}^{k=\frac{\pi}{2}} \frac{dz_k}{z_k} \quad (13)$$

here $z_k = \text{Det}(\mathcal{A})$, and we note that $\mathcal{A}(k) = \mathcal{E}_k \rho^1 \nu^0 \sigma^0 - t_{\perp} \rho^0 \nu^1 \sigma^0 - \mu \rho^0 \nu^0 \sigma^0 - h \rho^0 \nu^0 \sigma^3 + i \mathcal{L}_k \rho^1 \nu^0 \sigma^2 + \eta \rho^0 \nu^2 \sigma^1 - m_0 \rho^3 \nu^0 \sigma^3 + i \Delta \rho^0 \nu^0 \sigma^2$ is the 8×8 matrix.

III. RESULTS AND DISCUSSION

Let us briefly review the results obtained for a ideal one dimensional (1D) chain with AFM order. Here we focus on the study presented in Ref. [28]. This system corresponds to the one presented in Sec. II with $t_{\perp} = \eta = 0$ (accompanied by removal of ν basis from the tensor product). The topological phase diagram can be determined by the winding number \mathcal{W} . In the absence of magnetic order, the edge of topological region can be well described by the $h_c(\mu) = \sqrt{(-2t - \mu)^2 + \Delta^2}$ [21–23]. For fixed μ , the topological phase is realized for $|h| > h_c(\mu)$, which corresponds to the topologically non-trivial regions in the form of parabolas in $h-\mu$ phase diagram. However, the introduction of AFM magnetic order leads to the emergence of new region in the phase diagram (along diagonal

directions $h = \pm\mu$, as shown on Fig. 3). Due to negative ‘‘interference’’ with the old topological region, the new trivial part occur inside it. Simultaneously, new parts of topological region can be found outside of the old topological region. In practice, the size of such regions is controlled by the amplitude of magnetic moments. When the magnetic moments are large enough, the topological regions can be realized even at half-filling ($\mu = 0$) and in absence of external magnetic field ($h = 0$).

A. Topological phase diagrams for ladder

The topological phase diagram for ladder in the presence of relatively weak couplings (associated with the parameters t_{\perp} and η) between the chains within the ladder is presented in Fig. 4. Results are obtained using the same parameters for the chains as the ones used in Fig. 3, while the interchain couplings is set to $t_{\perp} = 0.2t$ and $\eta = 0.2\lambda$. As we can see, the phase diagram exhibits topological regions ‘‘splitted’’ with respect to the ones observed for the 1D AFM chain [cf. Fig. 3 and Fig. 4]. Such splitting is associated with a shift of the topological phase boundary within the chemical potential channel. Additionally, the winding number \mathcal{W} is no longer limited to values $-1, 0$, or 1 , and can be equal to -2 or 2 . This suggests an increase in the number of possible localized topological states in the ladder compared to the simple chain as expected.

Such behavior can be explained by analysing the block matrix $\mathcal{A}(k)$ used to calculate the winding number \mathcal{W} [see Eqs. (12) and (13)]. \mathcal{W} is evaluated using the determinant of $\mathcal{A}(k)$, hence changing the basis does not affect the result. By changing the order of the tensor product

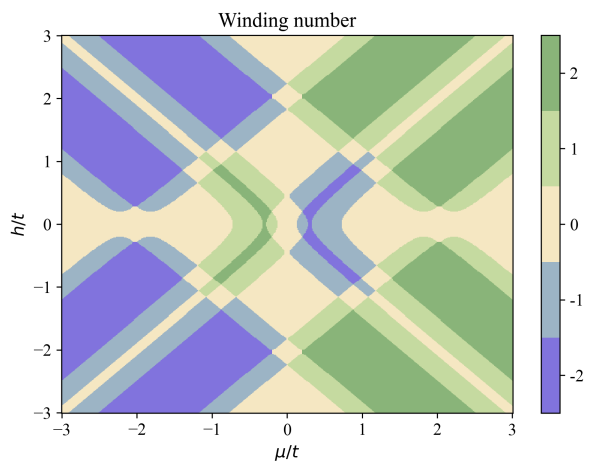


FIG. 4. The topological phase diagram of the ladder with AFM-like order. Results for the same parameters as Fig. 3, while coupling between chains within ladder is set as $t_{\perp}/t = 0.2$ and $\eta/\lambda = 0.2$.

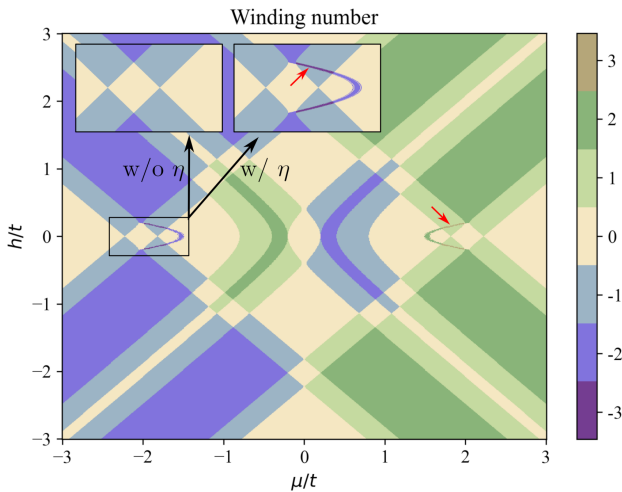


FIG. 5. The same as Fig. 4 for $\Delta/t = 0.0015$. Inset show zoom of marked area in the absence and presence of the inter-chain spin-orbit coupling η (left and right inset, respectively).

basis $(\nu, \sigma) \rightarrow (\sigma, \nu)$, we can rewrite $\mathcal{A}(k)$ as:

$$\begin{aligned} \mathcal{A}(k) &= (\mathcal{E}_k \rho^1 \sigma^0 - \mu \rho^0 \sigma^0 - h \rho^0 \sigma^3 + i \mathcal{L}_k \rho^1 \sigma^2 \\ &\quad - m_0 \rho^3 \sigma^3 + i \Delta \rho^0 \sigma^2) \nu^0 - t_{\perp} \rho^0 \sigma^0 \nu^1 + \eta \rho^0 \sigma^1 \nu^2 \\ &= \mathcal{A}_0 \nu^0 - t_{\perp} \rho^0 \sigma^0 \nu^1 + \eta \rho^0 \sigma^1 \nu^2, \end{aligned} \quad (14)$$

where \mathcal{A}_0 is the off diagonal block of the 1D AFM chain [28]. Using the properties of block diagonal matrices we can simplify the determinant of the block diagonal matrix \mathcal{A}

$$\det(\mathcal{A}) = \det(\mathcal{A}_0) \det(\mathcal{A}_0 - T \mathcal{A}_0^{-1} T^\dagger), \quad (15)$$

where $T = -t_{\perp} \rho^0 \sigma^0 - i \eta \rho^0 \sigma^1$ and $T^\dagger = -t_{\perp} \rho^0 \sigma^0 +$

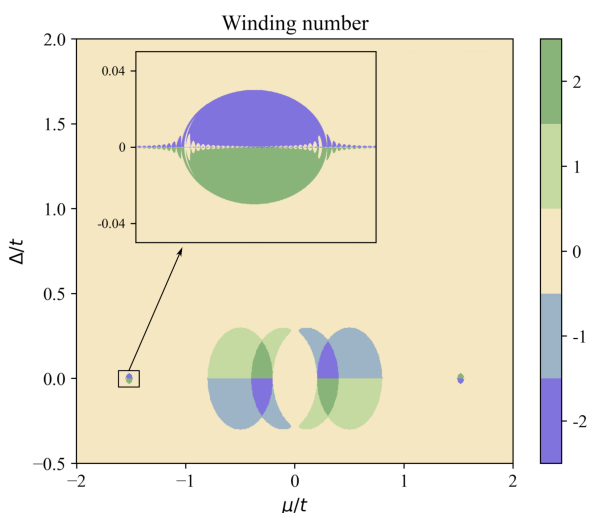


FIG. 6. Crossection of the topological phase diagram presented on Fig. 4 for $h = 0$.

$i \eta \rho^0 \sigma^1$. Hence we get

$$\det(\mathcal{A}) = \det(\mathcal{A}_0^2 - \mathcal{A}_0 T \mathcal{A}_0^{-1} T^\dagger). \quad (16)$$

Assuming $\eta = 0$,

$$\begin{aligned} \det(\mathcal{A}) &= \det(\mathcal{A}_0^2 - t_{\perp}^2 \rho^0 \sigma^0) \\ &= \det(\mathcal{A}_0 - t_{\perp} \rho^0 \sigma^0) \cdot \det(\mathcal{A}_0 + t_{\perp} \rho^0 \sigma^0) \\ &= \det[\mathcal{A}_0(\mu - t_{\perp})] \cdot \det[\mathcal{A}_0(\mu + t_{\perp})]. \end{aligned} \quad (17)$$

This equality shows that in the absence of Rashba SOC between the wires (η) the phase diagram as well as the winding number can be reproduced by superimposing two single wire phase diagrams and their corresponding winding numbers. This immediately implies the existence of winding number $\mathcal{W} \pm 2$. The winding number is still an odd function of the chemical μ , while an even function of the Zeeman field h , which was already reported for uncoupled 1D chains.

Features discussed above demonstrate the crucial role of the SOC η in the topological phase diagram. For example, the phase diagram can be tuned by the coupling between chains (via the hopping t_{\perp} and the SOC η). Nevertheless, the SOC η leads to occurrence of new non-trivial parts in the phase diagram. These properties can be observed by comparing the phase diagrams with or without the SOC η . An example is presented in Fig. 5 where the main structure of the phase diagram remains unchanged (cf. Fig. 4). However, the introduction of the SOC η leads to new topologically non-trivial regions around $\mu/t = \pm 2$ (cf. insets on Fig. 5). Moreover, these regions can exist even for infinitesimal magnetic fields. Similar behavior was already present in the case of the AFM chain close to the half-filling region (around $\mu = 0$) [28]. However, contrary to the AFM chain, higher winding numbers are found for ladders (like $\mathcal{W} = \pm 3$ in small topological region marked by red arrows on Fig. 5). Furthermore, we observed two effects in Fig. 7: i) a splitting of topological regions around half-filling and ii) the emergence of new topological regions close to the nearly empty/occupied band (i.e. close to the bottom/top of band, $\mu/t = \pm 2$).

Further tuning of the coupling between the chains can lead to more complicated phase diagrams. Indeed, the phase diagram for a larger interchain coupling ($t = t_{\perp}$ and $\lambda = \eta$) is presented in Fig. 7. Similar to the 1D chain, the non-trivial topological region exhibits parabolic boundaries for small h . However, contrary to the simple chain, increasing magnetic field result in parts with larger winding numbers $\mathcal{W} \pm 2$ and $\mathcal{W} \pm 3$. Additionally, close to $h/t = \pm 1$, we encounter a thin region of winding number ± 3 . These regions exhibit complex substructures when examined closely [see Figs. from 7(a) to 7(d)]. In fact, we find in Fig. 7(d) that the winding numbers $\mathcal{W} = 0$ to $\mathcal{W} = -3$ coexist in very close proximity.

The topological phase is very sensitive to the system parameters, and can exhibit fractal-like behavior. In fact, similar behavior can be found for different sets of system

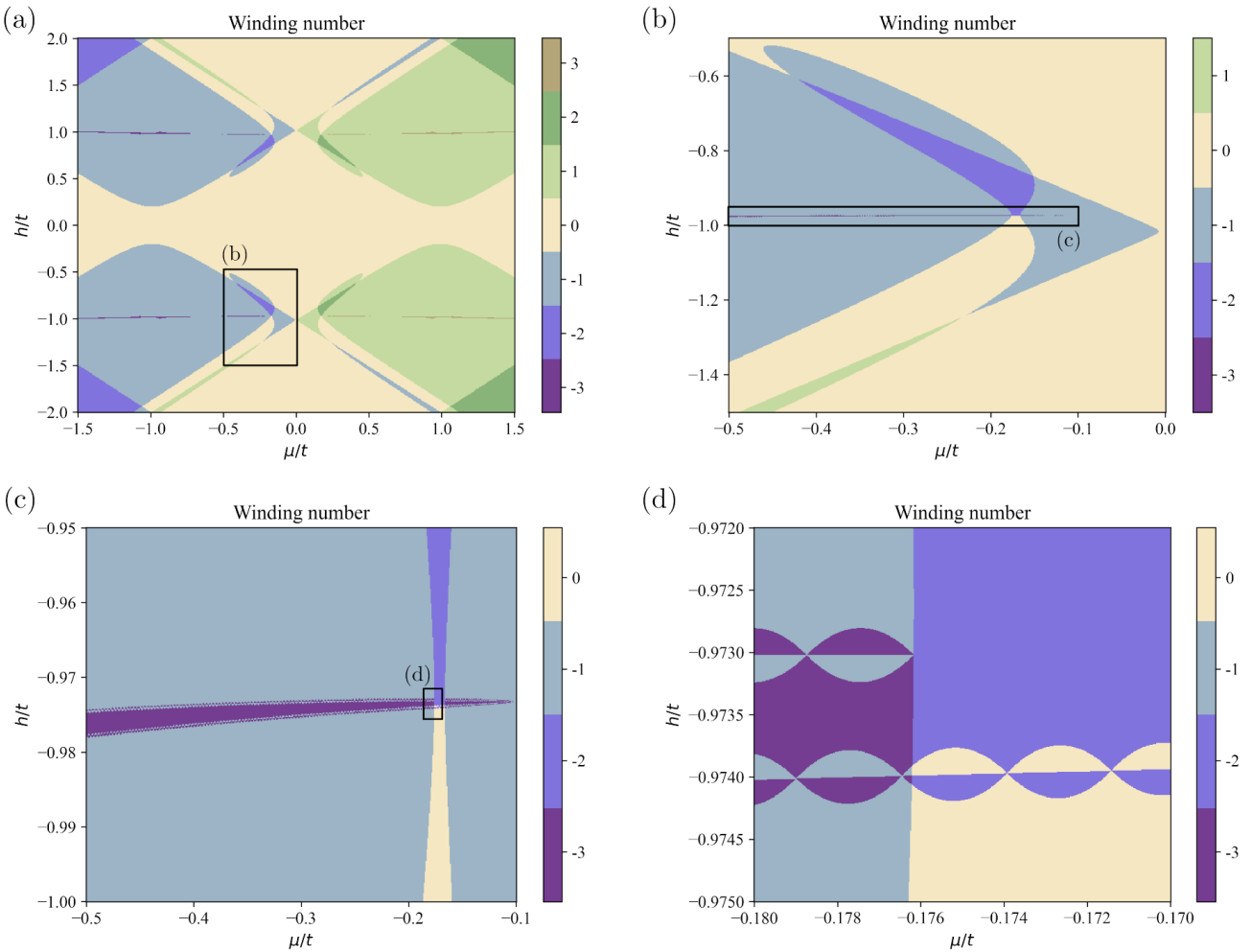


FIG. 7. The topological phase diagram of the ladder with AFM-like order. Next panels show zoom on marked area (as labeled). Results obtained for $t_{\perp}/t = 1$, $\Delta/t = 0.2$, $m_0/t = 0.1$, and $\lambda = \eta = -0.15t$.

parameters. For example Fig. 8 show the phase diagram for $h/t = 0.975$, while magnetic moment value m_0 is parameter. In this case, the nontrivial range of phase diagram with wild range of the winding number \mathcal{W} is present. We can notice that regions with larger \mathcal{W} are realized in smaller range of parameters. Nevertheless, for small values of magnetic moment m_0 , the phase diagram exhibits fractal-like feature with comb-like structure [Fig. 8(b)]. Parts of phases with $\mathcal{W} = -1$ and -3 are alternating along constant magnetization $m_0 = \text{const.}$ cross-sections.

B. Band inversions and spectral function

The transition from trivial to topological phase can be investigated within the band inversion formulation. In fact, the system band structure is given by the eigenvalue problem of the Hamiltonian in the matrix form (11). Thus, bands can be investigated within different subspace

(as mention in Sec. II) using the spectral function:

$$\mathcal{S}_{\mathbf{k}}(\omega) = -\frac{1}{\pi} \sum_{sw\sigma} \text{Im} \mathcal{G}_{\mathbf{k}sw\sigma}(\omega + i0^+), \quad (18)$$

where $\mathcal{G} = (\omega - \mathbb{H}_{\mathbf{k}})^{-1}$ is the Green function. The spectral function $\mathcal{S}_{\mathbf{k}}(\omega)$ can be then reexpressed in terms of the momentum space Bogoliubov–de Gennes (BdG) equations, as follows:

$$\begin{aligned} \mathcal{S}_{\mathbf{k}}(\omega) &= \sum_{sw\sigma} \mathcal{S}_{\mathbf{k}sw\sigma}(\omega) \\ &= \sum_{\mathbf{k}sw\sigma n} [|u_{\mathbf{k}sw\sigma}^n|^2 \delta(\omega - \mathcal{E}_n) + |v_{\mathbf{k}sw\sigma}^n|^2 \delta(\omega + \mathcal{E}_n)], \end{aligned} \quad (19)$$

where $u_{\mathbf{k}sw\sigma}^n$ and $v_{\mathbf{k}sw\sigma}^n$ are particle and hole part of the n th eigenvector of the BdG equations of $\mathbb{H}_{\mathbf{k}}$ (11). Here, n denotes the band index out of a total of 16 bands with energies \mathcal{E}_n . The contribution of the different subspaces to different bands can be indicated by (A and B) sublattice, (α and β) wire, (\uparrow and \downarrow) spin-dependent (partial)

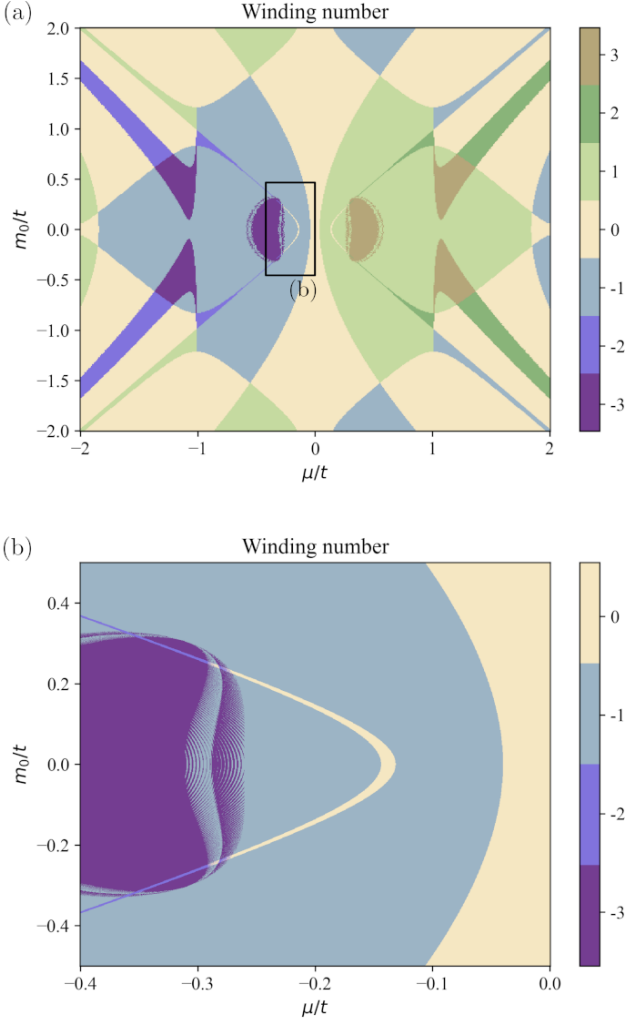


FIG. 8. The topological phase diagram of the ladder with AFM-like order. Panel (b) shows zoom on marked area at panel (a). Results obtained for $t_{\perp}/t = 1$, $\Delta/t = 0.2$, $h/t = -0.975$, and $\lambda = \eta = -0.15t$.

spectral function:

$$\delta\mathcal{S}_k^s = \mathcal{S}_{kA\alpha\uparrow} + \mathcal{S}_{kA\alpha\downarrow} + \mathcal{S}_{kB\beta\uparrow} + \mathcal{S}_{kB\beta\downarrow} - \mathcal{S}_{kB\alpha\uparrow} - \mathcal{S}_{kB\alpha\downarrow} - \mathcal{S}_{kB\beta\uparrow} - \mathcal{S}_{kB\beta\downarrow}, \quad (20)$$

$$\delta\mathcal{S}_k^w = \mathcal{S}_{kA\alpha\uparrow} + \mathcal{A}_{kA\alpha\downarrow} + \mathcal{S}_{kB\alpha\uparrow} + \mathcal{S}_{kB\alpha\downarrow} - \mathcal{S}_{kB\beta\uparrow} - \mathcal{S}_{kB\beta\downarrow} - \mathcal{S}_{kA\beta\uparrow} - \mathcal{S}_{kA\beta\downarrow} - \mathcal{S}_{kB\beta\uparrow} - \mathcal{S}_{kB\beta\downarrow}, \quad (21)$$

$$\delta\mathcal{S}_k^{\sigma} = \mathcal{S}_{kA\alpha\uparrow} + \mathcal{S}_{kB\alpha\uparrow} + \mathcal{S}_{kB\beta\uparrow} + \mathcal{S}_{kB\beta\downarrow} - \mathcal{S}_{kA\alpha\downarrow} - \mathcal{S}_{kB\alpha\downarrow} - \mathcal{S}_{kB\beta\downarrow} - \mathcal{S}_{kB\beta\uparrow}. \quad (22)$$

It is evident from the form of these differential spectral functions that each of these quantities measure the imbalance of the contribution from their respective subspace and therefore allows for a careful analysis and labelling of the different phases. Additionally, the band polarization which refers to the absolute sign of the partial spectral function, $\delta\mathcal{S}_k$ changes as we cross boundary between different phases (in sense of the winding number).

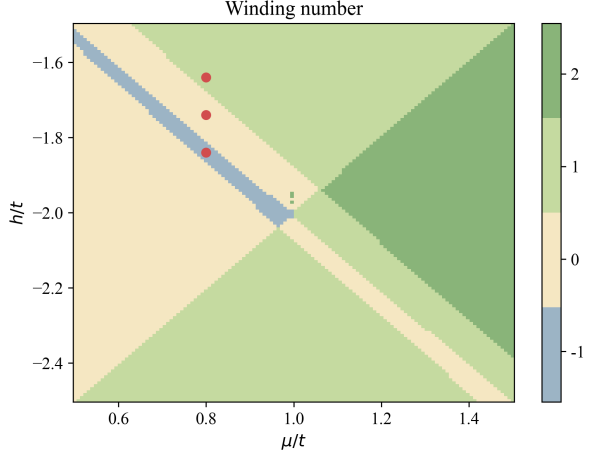


FIG. 9. The phase diagram of the winding number for μ vs h . The magnetic moment $m_0 = -0.1t$, superconducting order $\Delta = -0.2t$, and as before $\lambda = \eta = -0.15t$ along with $t = t_{\perp}$. The red dots are the points in the phase diagram which have been chosen to display the band inversion located at $\mu = 0.8$ and $h/t = -1.84$, -1.74 , and -1.64 (bottom to top).

To illustrate the use of these differential spectral functions, we analyse the part of the phase diagram where we observe transitions between different phases in Fig. 9. We choose specific points marked by red dots in Fig. 9, characterized by different winding numbers ($-1, 0$, and 1 , for fixed chemical potential $\mu/t = 0.8$ and magnetic fields $h/t = -1.84$, -1.74 , and -1.64 , respectively). Increasing magnetic field leads to two phase transitions: from nontrivial to trivial phase ($-1 \rightarrow 0$), and from trivial to nontrivial phase ($0 \rightarrow 1$). We begin with the sublattice contribution $\delta\mathcal{S}_k^s$ which is shown in Fig. 10(a). Beyond the Lifshitz transition at $\mathbf{k} = 0$ (initially unoccupied cross the Fermi level) induced by increasing the magnetic field, we observed leaking of the sublattice contribution between bands at $\mathbf{k} = \pm\pi/2$. Thus, the sublattice contribution to the bands is changed from $(0,1,0,1)$ to $(1,0,1,0)$ to $(1,1,0,0)$ for bands from lowest to highest energies around the Fermi level. However, independent of \mathcal{W} , bands exhibit strong sublattice polarization without clear inversion. Situation is better suited for interpretation in the case of the wire contribution $\delta\mathcal{S}_k^w$ around $\mathbf{k} = \pm\pi/2$, presented on Fig. 10(b). Initially two bands exhibit strong wire polarization, which after increasing the magnetic field leads to modification of the subchain contribution from $(0,1,0,-1)$ to $(1,0,-1,0)$ to $(1,-1,0,0)$. In general we see that the band structure analyses is more complicated than in single chain, due to the more complex band structure (which now contain 16 sub-bands). However by help of the differential spectral functions, one can understand these transitions.

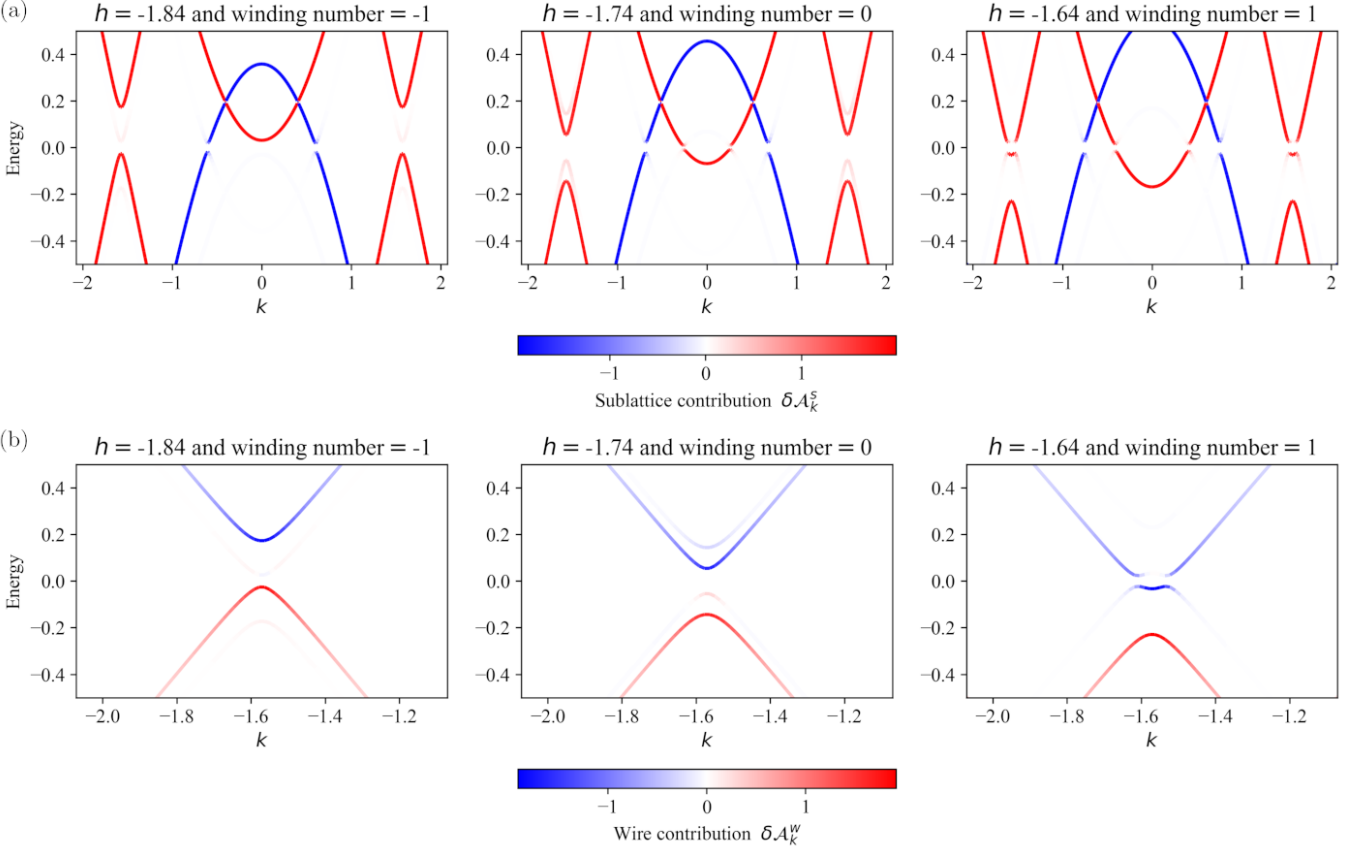


FIG. 10. The energy bands graded with the differential spectral function for the (a) sublattice and (b) wire. The energy bands have been plotted for the parameter value marked red in Fig. 9

IV. REAL SPACE INVESTIGATION

In this section we will investigate the edge modes in real space ladder with finite number of sites. To diagonalize the real space Hamiltonian [from Eqs. (1) to (4)], we use the Bogoliubov–Valatin transformation [60]:

$$c_{isw\sigma} = \sum_n (u_{isw\sigma}^n \gamma_n - \sigma v_{isw\sigma}^{n*} \gamma_n^\dagger), \quad (23)$$

where γ_n and γ_n^\dagger are the fermionic operators. This transformation leads to a real space BdG equations in the form [28, 61–63]:

$$\mathcal{E}_n \Psi_a^n = \sum_b \mathbb{H}_{ab} \Psi_b^n, \quad (24)$$

where \mathcal{E}_n and $\Psi_{a=isw\sigma}^n = (u_{isw\sigma}^n \ v_{isw\sigma}^n)$ denotes n th eigenpair of real space Hamiltonian \mathbb{H}_{ab} in matrix form. Using the BdG equations solution, the local density of states (LDOS) $\rho_{isw\sigma} = -1/\pi \text{Im} \langle \langle c_{isw\sigma} | c_{isw\sigma}^\dagger \rangle \rangle$ can be express as:

$$\begin{aligned} \rho_{isw} &= \sum_{n\sigma} [|u_{isw\sigma}^n|^2 \delta(\omega - \mathcal{E}_n) + |v_{isw\sigma}^n|^2 \delta(\omega + \mathcal{E}_n)] \\ &= \sum_n \rho_{isw}^n. \end{aligned} \quad (25)$$

Experimentally measured tunneling amplitudes using a scanning tunneling microscope (STM) gives the information about the edge modes in the system. The LDOS provides a theoretical path of gaining similar insights for our system.

In the real space description, the number of sites play an important role in the obtained results (see also Sec. IV A) [28]. In this part we investigate system with 201 sites along ladder. This gives the ladder with the same sublattice at both ends of system (i.e. sequence $A-B-\cdots-B-A$). We exactly diagonalize the Hamiltonian which gives the energy spectra for the system. In order to gain more insight about the bound states we vary the magnetic field h , or the chemical potential μ , as shown in Fig. 11. In both cases, $h = \text{const.}$ and $\mu = \text{const.}$ across trivial and non-trivial phases. Indeed, for example for Figs. 11(a) and 11(b), a typical behavior is observed: The increase of the magnetic field leads to the closing of the trivial gap and reopening of a new topological gap. Therefore, for some range of h , zero-energy in-gap Majorana modes are observed. However, as we mentioned earlier, realization of the topological phase strongly depends on the system parameters. For example, around $h/t = 1$ at Fig. 11(a), we observe lifting of the zero-modes degeneracy, and destruction of the topological phase. Con-

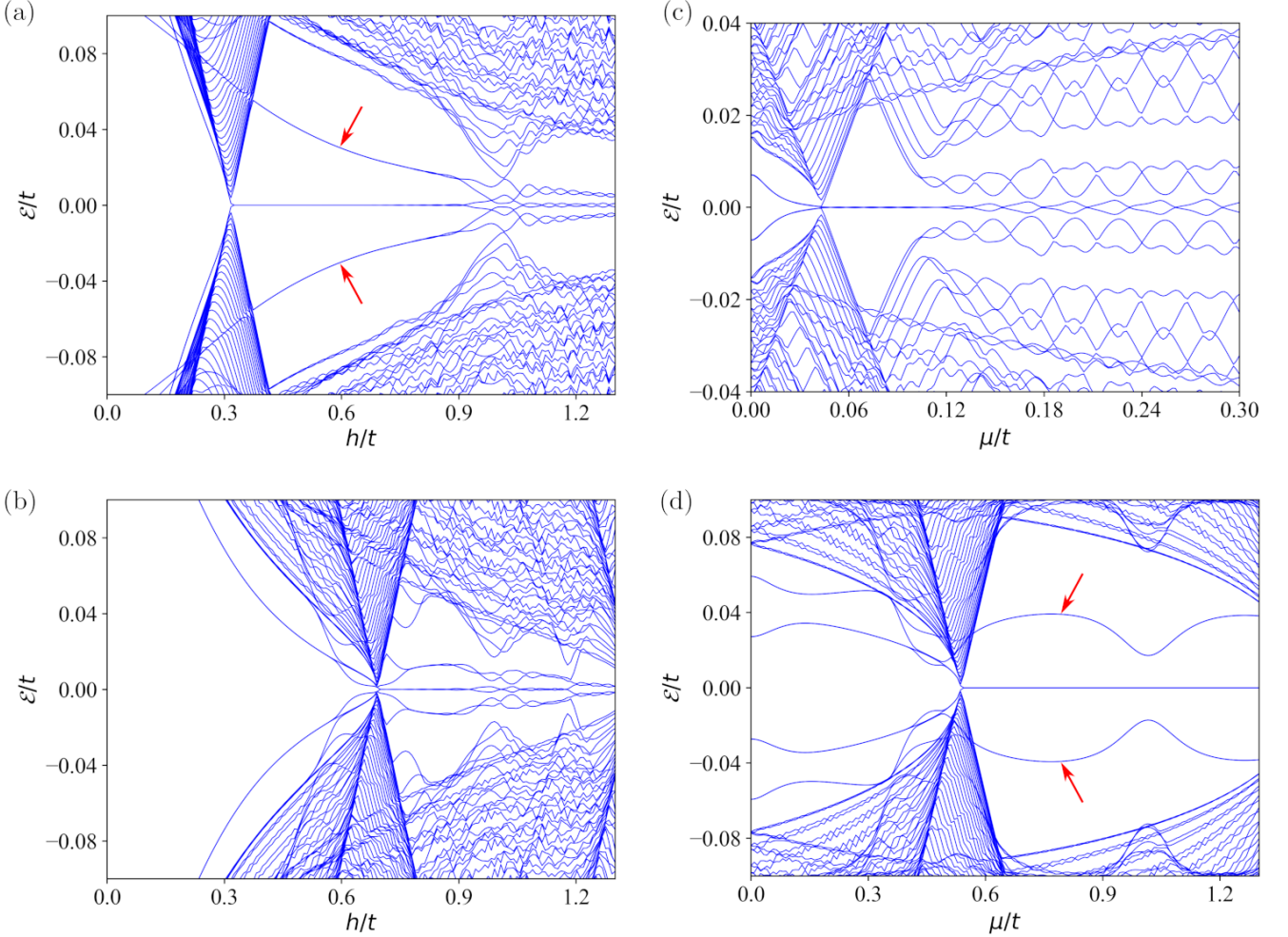


FIG. 11. Spectrum of the system with 201 sites along ladder, obtained from direct diagonalization of the Bogoliubov–de Gennes equations in real space. Results obtained for $m_0/t = 0.1$, $\lambda = \eta = 0.15t$, $\Delta/t = -0.2$, and $t_\perp = t$. Results for fixed $\mu/t = 1/3$ (a), and fixed $h/t = 0.5$ (b).

trary to the 1D chain, the number of in-gap states is not limited to one pair with zero-energy, i.e. Majorana edge modes. In some situation, additional in-gap states can be observed in the topological phase [marked by red arrow on Figs. 11(a) or 11(d)].

A. Even–odd behavior

The system spectrum shows drastic difference depending on the even–odd length of the ladder. This is well visible when we compare the spectrum for system with comparable length. We choose 200 and 201 sites, and the results are presented in Fig. 12. The topological in-gap zero energy Majorana edge modes (marked by red arrows) are independent of the length, which directly show their topological nature. However, there are also states, whose existence or degeneracy strongly depends on the system length. Such even–odd behavior is directly as-

sociated with the magnetic order and therefore affects the observed LDOS. For an odd number of sites, both edges cannot be distinguished via the site-inversion symmetry with respect to the mirror symmetry (when magnetic order realized sequence A-B-⋯-B-A or sequence B-A-⋯-A-B). Similar symmetry cannot be realized in the case of an even number of sites (ladder with sequence A-B-⋯-A-B). Additionally, this even–odd behavior affects the degenerate states in the whole range of parameters (e.g. states marked by green arrow on Fig. 12).

Similarly to the single AFM chain [28], the magnetic field leads to the breaking of symmetry between left and right edge of the ladder resulting in the particle imbalance at both ends of the ladder. The so-obtained LDOS are presented in Fig. 13 for two pairs of double-degenerated non-zero in-gap states, while in Fig. 14 for one pair of in-gap zero energy Majorana edge modes. Top and bottom parts of panels, correspond to the subchain α and β , respectively, while blue and orange lines to sub-

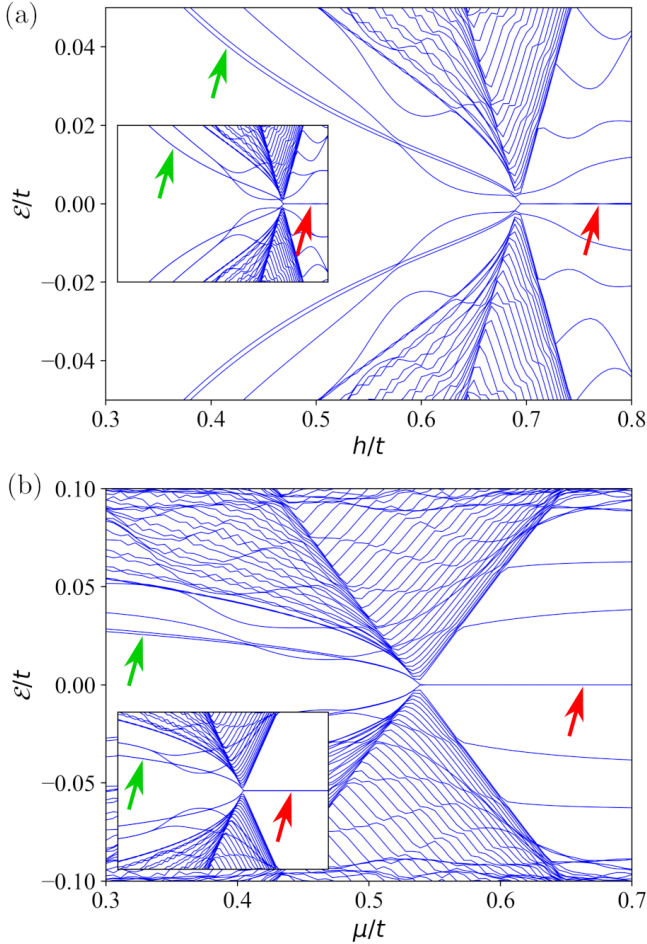


FIG. 12. The same as Fig. 11 for different length of the subchains. Energy spectrum for 202 sites is presented on main panels, while insets show results for 201 sites. Results obtained for $m_0/t = 0.1$, $\lambda/t = \eta/t = 0.15$, $\Delta/t = -0.2$, and $t_\perp = t$. Results for fixed $\mu/t = 1/3$ (a), and fixed $h/t = 0.5$ (b).

lattice A and B, respectively. As we mentioned earlier, for an even number of sites, there is strong difference between both sites [left panels on Fig. 13, and Fig. 14(a)]. Contrary to this, a ladder with an odd number of sites exhibits left-right symmetry. However, We should notice, that this symmetry is not preserved within the same lattice, but between subchains α and β , i.e. left (right) site of subchain α is the same as right (left) site of subchain β . This is true for an odd number of sites, independent of the energies of discussed in-gap states [right panels in Fig. 13, and Fig. 14(b)].

This observation can be associated with the existence of a center of crystalline symmetry (an inversion) in the case of an odd number of sites along the subchains. However, this center of crystalline symmetry do not only affect sites number within the (sub)chains, like in the AFM chain [28], but also the subchains itself, i.e. $\alpha \leftrightarrow \beta$ [see Sec. IV A]. Thus, the left end of the α (β) subchain, can

be transformed to right end of β (α) subchain, with simultaneous changes of the SOCs directions ($\lambda \rightarrow -\lambda$ and $\eta \rightarrow -\eta$). The magnetic moments in A and B sublattice, as well as direction magnetic field h or spin \uparrow/\downarrow quantization axis, are unchanged.

Contrary to the zero energy modes the degenerate massive modes are not topologically protected. Albeit, in the limit where the number of rungs in the ladder tend to infinitum, the topological phase illustrates that there are parameters regimes with non-zero winding number. The absence of corresponding additional zero-energy modes in the finite system suggests a transition from multiple Majorana modes (infinite ladder) to phases with a single Majorana mode and massive fermionic modes (finite ladder).

V. SUMMARY AND OUTLOOK

Topological phase realized in chains with ferromagnetic or antiferromagnetic order in proximity of a superconductor can lead to topologically protected Majorana edge modes. Recently, such feature was discussed in several systems where topological phases were observed in wide ranges of system parameters.

In this paper we have investigated the topological phase diagrams of a block magnetic ladder. In the case of weak coupling between subchains, the topological phase diagram is very similar to the one reported earlier for antiferromagnetic chains. However, a topological phase exist in doubled region exhibiting negative or/and positive interference. Consequently, absolute value of the winding number is not limited to ≤ 1 like in chains, and is ≤ 3 in our model of the block ladder. Additionally, the SOC between chains is responsible for the realization of new topological phases. Similarly, like in the antiferromagnetic chain, the topological phase can exist even in the absence of the magnetic field, or around half-filling (far from bottom or top of band).

For strongly coupled subchains, the topological phase diagrams becomes more complex. and is very sensitive to the system parameters. Additionally, the topological phase diagram often exhibits a fractal-like structure around boundaries between phases with different winding numbers. Thus, contrary to the ferromagnetic chain, the condition for realization of the topological phase cannot be given analytically using a closed analytic formula.

Finally, we check that the topological phases are associated with the realization of in-gap edge modes. Some of them can be classified as zero energy Majorana edge modes. However, for phases with absolute value of the winding numbers larger than 1, we have found additional non-zero energy in-gap states localized at the edges of the subchains. Finally, such in-gap states exhibit an even-odd behavior with respect to the number of sites within the subchains which is related to the presence or absence of inversion symmetry in the crystal.

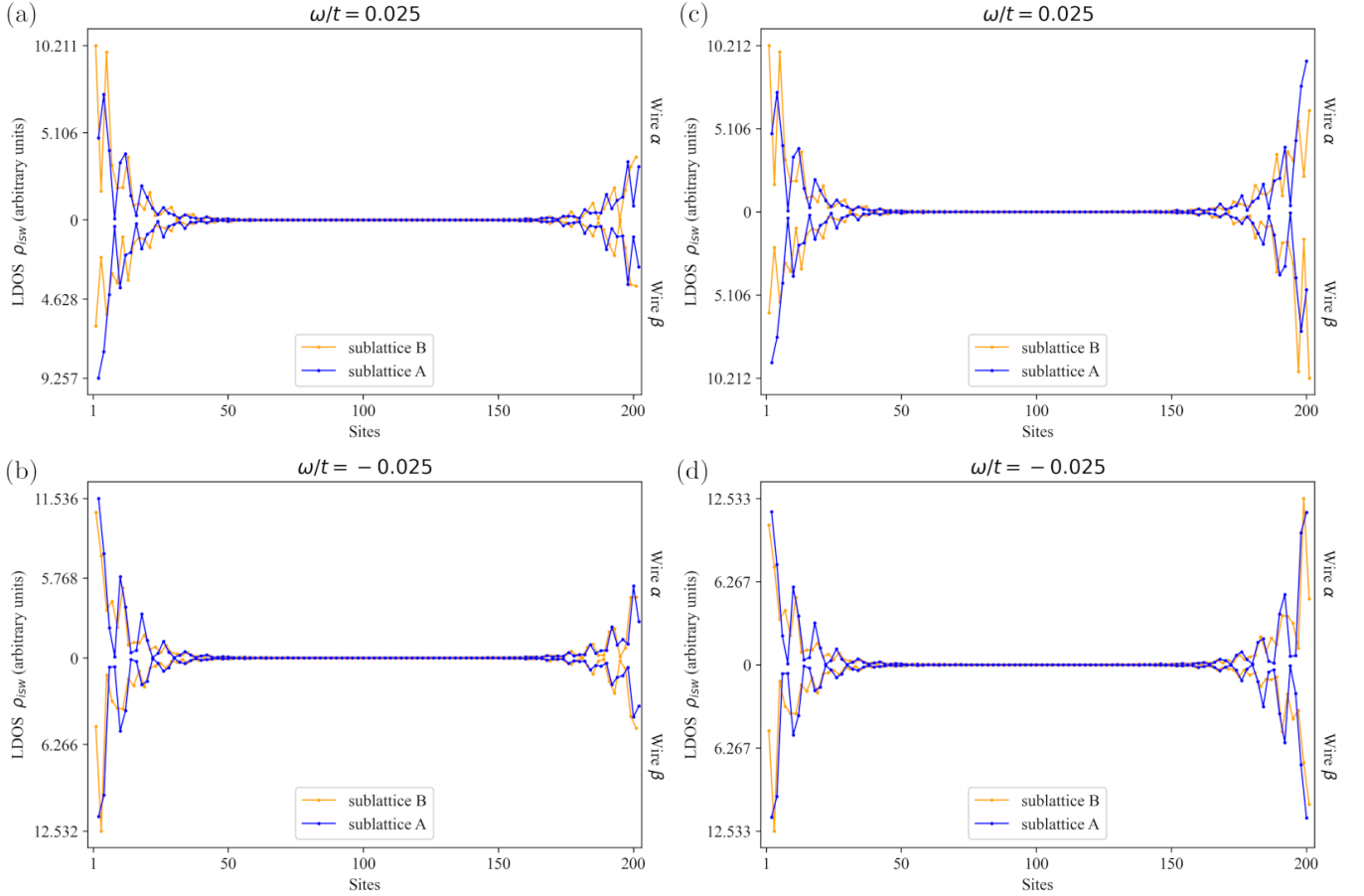


FIG. 13. LDOS for even (left column) and odd (right column) number of sites on either wire. The LDOS is calculated for energy spectrum shown in Fig. 12(b) at $\mu = 0.35t$. The LDOS is calculated in the trivial region of the spectra around or at the degenerated energy level i.e. $\omega = \pm 0.025t$.

ACKNOWLEDGMENTS

Some figures in this work were rendered using VESTA [64] software. S.Y. and A.P. are grateful to Laboratoire de Physique des Solides in Orsay (CNRS, University Paris Saclay) for hospitality during a part of the work on this project. S.Y. acknowledges financial support provided by the Polish National Agency for Academic Exchange NAWA under the Programme STER-Internationalisation of doctoral schools, Project no BPI/STE/2023/1/00027/U/00001. We kindly acknowledge the support by the National Science Centre (NCN, Poland) under Project No. 2021/43/B/ST3/02166.

Appendix A: Inversion symmetry for “odd” ladder

In this appendix we discuss the inversion symmetry in the system with odd number of sites along chains. The inversion symmetry with respect to the center of symmetry, would flip both site and subchain. This the site located at site i in subchain α is migrated to location

$j = N + 1 - i$ in subchain β (here N is the total number of sites in each subchains α and β). It is now fruitful to demonstrate the action of inversion operator acting on the Hamiltonian. The BdG Hamiltonian in real space (see Eq. 24), can be represent as a block-diagonal matrix:

$$\mathbb{H} = \begin{pmatrix} H & \Delta \\ \Delta^T & -H^* \end{pmatrix}, \quad (A1)$$

where H and Δ are block tri-diagonal matrices, and $\Delta^T = -\Delta$. Using the same representation as described in previous sections, we have:

$$H = \begin{pmatrix} D_1 & K & & & & & & \\ K^* & D_2 & K & & & & & \\ & K^* & D_3 & & & & & \\ & & & \ddots & & & & \\ & & & & D_{N-2} & K & & \\ & & & & & K^* & D_{N-1} & K \\ & & & & & & K^* & D_N \end{pmatrix}, \quad (A2)$$

where $K = -t\nu^0\sigma^0 - t_\perp\nu^1\sigma^0 - i\lambda\nu^0\sigma^1 - \eta\nu^2\sigma^1$ and $D_i = \mu\nu^0\sigma^0 - h\nu^0\sigma^3 + (-1)^i m_0\nu^0\sigma^3$ subblock are 4×4 matrices

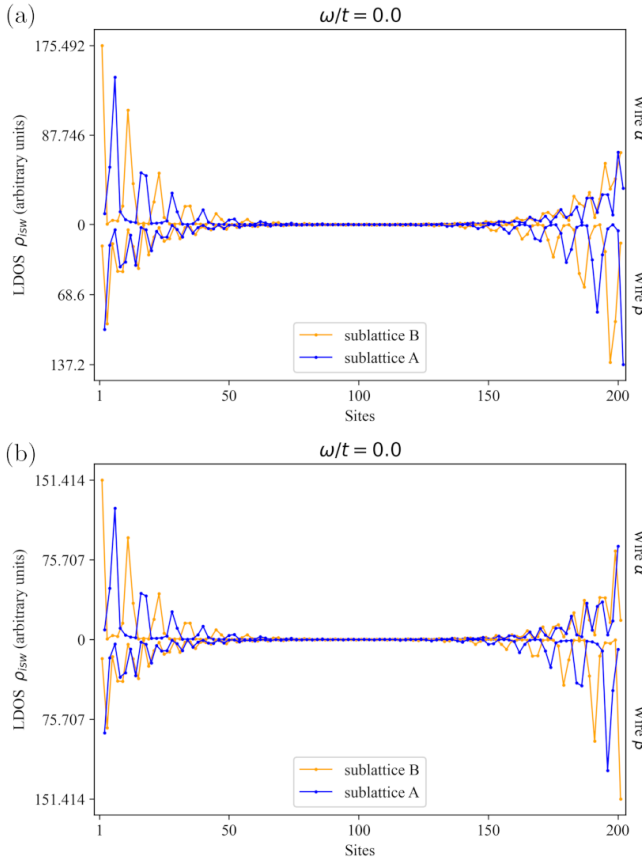


FIG. 14. LDOS for topological bands at zero energy for the energy spectrum in Fig. 12(a) at $h = -0.8t$ with even number of rungs in (a) and odd number of rungs in (b).

(index i denote site along ladder). The blocks represent

two sites one on each wire within the unit cell (hence half the unit cell). We note that K incorporates the hoppings and SOCs along and between subchains, while the sublattice information is built into the diagonal block D_i . Additionally, superconductivity is described by $\Delta = i\Delta\nu^0\sigma^2\mathbb{I}_N$.

Now, we are focused on the ladder composed of odd number of sites along subchains, what correspond to the magnetic order A-B- \cdots -B-A (or equivalently B-A- \cdots -A-B). The finite system real space Hamiltonian remains invariant under geometrical inversion applied along \hat{x} and \hat{y} directions (we assume subchains along \hat{x}), while the magnetic order is unchanged. We observe that inversion $H \rightarrow H^*$, on the other hand leaving Δ block unaffected. Thus, we can find the following operation:

$$\mathcal{I}\mathbb{H}\mathcal{I}^\dagger = \begin{pmatrix} H^* & \Delta \\ \Delta^T & -H \end{pmatrix}, \quad (A3)$$

where \mathcal{I} is the inversion operation given by:

$$\mathcal{I} = \tau^0 \times \begin{pmatrix} 0 & \sigma^0\nu^1 \\ \dots & \dots \\ \sigma^0\nu^1 & 0 \end{pmatrix}. \quad (A4)$$

Consequently, we can find the Hamiltonian of the ladder after inversion \mathbb{H}^{inv} , as:

$$\mathbb{H}^{\text{inv}} = \mathcal{I}\mathbb{H}\mathcal{I}^\dagger = - \begin{pmatrix} -H^* & -\Delta \\ -\Delta^T & H \end{pmatrix} = - \begin{pmatrix} -H^* & \Delta^T \\ \Delta & H \end{pmatrix} \quad (A5)$$

Such relation, combined with build-in particle-hole symmetry, implies that the inversion operation does not changes the spectrum.

[1] A. Y. Kitaev, Unpaired Majorana fermions in quantum wires, *Phys.-Usp.* **44**, 131 (2001).

[2] R. Aguado, Majorana quasiparticles in condensed matter, *Riv. Nuovo Cim.* **40**, 523 (2017).

[3] R. M. Lutchyn, E. P. A. M. Bakkers, L. P. Kouwenhoven, P. Krogstrup, C. M. Marcus, and Y. Oreg, Majorana zero modes in superconductor–semiconductor heterostructures, *Nature Reviews Materials* **3**, 52 (2018).

[4] R. Pawlak, S. Hoffman, J. Klinovaja, D. Loss, and E. Meyer, Majorana fermions in magnetic chains, *rog. Part. Nucl. Phys.* **107**, 1 (2019).

[5] T.-P. Choy, J. M. Edge, A. R. Akhmerov, and C. W. J. Beenakker, Majorana fermions emerging from magnetic nanoparticles on a superconductor without spin-orbit coupling, *Phys. Rev. B* **84**, 195442 (2011).

[6] S. Nadj-Perge, I. K. Drozdov, B. A. Bernevig, and A. Yazdani, Proposal for realizing majorana fermions in chains of magnetic atoms on a superconductor, *Phys. Rev. B* **88**, 020407 (2013).

[7] F. Pientka, L. I. Glazman, and F. von Oppen, Topological superconducting phase in helical Shiba chains, *Phys. Rev. B* **88**, 155420 (2013).

[8] B. Braunecker and P. Simon, Interplay between classical magnetic moments and superconductivity in quantum one-dimensional conductors: Toward a self-sustained topological majorana phase, *Phys. Rev. Lett.* **111**, 147202 (2013).

[9] J. Klinovaja, P. Stano, A. Yazdani, and D. Loss, Topological superconductivity and Majorana fermions in RKKY systems, *Phys. Rev. Lett.* **111**, 186805 (2013).

[10] M. M. Vazifeh and M. Franz, Self-organized topological state with Majorana fermions, *Phys. Rev. Lett.* **111**, 206802 (2013).

[11] B. Braunecker and P. Simon, Self-stabilizing temperature-driven crossover between topological and nontopological ordered phases in one-dimensional conductors, *Phys. Rev. B* **92**, 241410 (2015).

[12] G. M. Andolina and P. Simon, Topological properties of

chains of magnetic impurities on a superconducting substrate: Interplay between the Shiba band and ferromagnetic wire limits, *Phys. Rev. B* **96**, 235411 (2017).

[13] V. Kaladzhyan, P. Simon, and M. Trif, Controlling topological superconductivity by magnetization dynamics, *Phys. Rev. B* **96**, 020507 (2017).

[14] S. Nadj-Perge, I. K. Drozdov, J. Li, H. Chen, S. Jeon, J. Seo, A. H. MacDonald, B. A. Bernevig, and A. Yazdani, Observation of Majorana fermions in ferromagnetic atomic chains on a superconductor, *Science* **346**, 602 (2014).

[15] R. Pawlak, M. Kisiel, J. Klinovaja, T. Meier, S. Kawai, T. Glatzel, D. Loss, and E. Meyer, Probing atomic structure and Majorana wavefunctions in mono-atomic Fe chains on superconducting Pb surface, *npj Quantum Information* **2**, 16035 (2016).

[16] M. Ruby, B. W. Heinrich, Y. Peng, F. von Oppen, and K. J. Franke, Exploring a proximity-coupled Co chain on Pb(110) as a possible Majorana platform, *Nano Lett.* **17**, 4473 (2017).

[17] B. E. Feldman, M. T. Randeria, J. Li, S. Jeon, Y. Xie, Z. Wang, I. K. Drozdov, B. Andrei Bernevig, and A. Yazdani, High-resolution studies of the Majorana atomic chain platform, *Nat. Phys.* **13**, 286 (2017).

[18] S. Jeon, Y. Xie, J. Li, Z. Wang, B. A. Bernevig, and A. Yazdani, Distinguishing a Majorana zero mode using spin-resolved measurements, *Science* **358**, 772 (2017).

[19] H. Kim, A. Palacio-Morales, T. Posske, L. Rózsa, K. Palotás, L. Szunyogh, M. Thorwart, and R. Wiesendanger, Toward tailoring Majorana bound states in artificially constructed magnetic atom chains on elemental superconductors, *Sci. Adv.* **4**, eaar5251 (2018).

[20] A. Kobialka, P. Piekarz, A. M. Oleś, and A. Ptak, First-principles study of the nontrivial topological phase in chains of 3d transition metals, *Phys. Rev. B* **101**, 205143 (2020).

[21] M. Sato, Y. Takahashi, and S. Fujimoto, Non-Abelian topological order in *s*-wave superfluids of ultracold fermionic atoms, *Phys. Rev. Lett.* **103**, 020401 (2009).

[22] M. Sato and S. Fujimoto, Topological phases of noncentrosymmetric superconductors: Edge states, Majorana fermions, and non-Abelian statistics, *Phys. Rev. B* **79**, 094504 (2009).

[23] M. Sato, Y. Takahashi, and S. Fujimoto, Non-Abelian topological orders and Majorana fermions in spin-singlet superconductors, *Phys. Rev. B* **82**, 134521 (2010).

[24] J. D. S. Bommer, H. Zhang, O. Güll, B. Nijholt, M. Wimmer, F. N. Rybakov, J. Garaud, D. Rodic, E. Babaev, M. Troyer, D. Car, S. R. Plissard, E. P. A. M. Bakkers, K. Watanabe, T. Taniguchi, and L. P. Kouwenhoven, Spin-orbit protection of induced superconductivity in Majorana nanowires, *Phys. Rev. Lett.* **122**, 187702 (2019).

[25] W. S. Cole, S. Das Sarma, and T. D. Stanescu, Effects of large induced superconducting gap on semiconductor Majorana nanowires, *Phys. Rev. B* **92**, 174511 (2015).

[26] T. D. Stanescu and S. Das Sarma, Proximity-induced low-energy renormalization in hybrid semiconductor-superconductor Majorana structures, *Phys. Rev. B* **96**, 014510 (2017).

[27] A. Heimes, P. Kotetes, and G. Schön, Majorana fermions from shiba states in an antiferromagnetic chain on top of a superconductor, *Phys. Rev. B* **90**, 060507 (2014).

[28] A. Kobialka, N. Sedlmayr, and A. Ptak, Majorana bound states in a superconducting Rashba nanowire in the presence of antiferromagnetic order, *Phys. Rev. B* **103**, 125110 (2021).

[29] M. Steinbrecher, R. Rausch, K. T. That, J. Hermenau, A. A. Khajetoorians, M. Potthoff, R. Wiesendanger, and J. Wiebe, Non-collinear spin states in bottom-up fabricated atomic chains, *Nat. Commun.* **9**, 2853 (2018).

[30] L. Schneider, P. Beck, T. Posske, D. Crawford, E. Mascot, S. Rachel, R. Wiesendanger, and J. Wiebe, Topological shiba bands in artificial spin chains on superconductors, *Nat. Phys.* **17**, 943 (2021).

[31] L. Schneider, P. Beck, L. Rózsa, T. Posske, J. Wiebe, and R. Wiesendanger, Probing the topologically trivial nature of end states in antiferromagnetic atomic chains on superconductors, *Nat. Commun.* **14**, 2742 (2023).

[32] L. Schneider, S. Brinker, M. Steinbrecher, J. Hermenau, T. Posske, M. dos Santos Dias, S. Lounis, R. Wiesendanger, and J. Wiebe, Controlling in-gap end states by linking nonmagnetic atoms and artificially-constructed spin chains on superconductors, *Nat. Commun.* **11**, 4707 (2020).

[33] L. Schneider, P. Beck, J. Neuhaus-Steinmetz, L. Rózsa, T. Posske, J. Wiebe, and R. Wiesendanger, Precursors of Majorana modes and their length-dependent energy oscillations probed at both ends of atomic Shiba chains, *Nature Nanotechnology* **17**, 384 (2022).

[34] H. Hong and H. Steinfink, The crystal chemistry of phases in the Ba-Fe-S and Se systems, *J. Solid State Chem.* **5**, 93 (1972).

[35] S. Dong, J.-M. Liu, and E. Dagotto, BaFe₂Se₃: A high *T_C* magnetic multiferroic with large ferrielectric polarization, *Phys. Rev. Lett.* **113**, 187204 (2014).

[36] W. Zheng, V. Balédent, M. B. Lepetit, P. Retailleau, E. V. Elslande, C. R. Pasquier, P. Auban-Senzier, A. Forget, D. Colson, and P. Foury-Leylekian, Room temperature polar structure and multiferroicity in BaFe₂Se₃, *Phys. Rev. B* **101**, 020101 (2020).

[37] W. G. Zheng, V. Balédent, L. Bocher, A. Forget, D. Colson, and P. Foury-Leylekian, Origin of spin-glass-like magnetic anomaly in the superconducting and multiferroic spin ladder BaFe₂Se₃, *Phys. Rev. B* **107**, 024423 (2023).

[38] H. Lei, H. Ryu, A. I. Frenkel, and C. Petrovic, Anisotropy in BaFe₂Se₃ single crystals with double chains of fese tetrahedra, *Phys. Rev. B* **84**, 214511 (2011).

[39] Y. Nambu, K. Ohgushi, S. Suzuki, F. Du, M. Avdeev, Y. Uwatoko, K. Munakata, H. Fukazawa, S. Chi, Y. Ueda, and T. J. Sato, Block magnetism coupled with local distortion in the iron-based spin-ladder compound BaFe₂Se₃, *Phys. Rev. B* **85**, 064413 (2012).

[40] V. Svitlyk, D. Chernyshov, E. Pomjakushina, A. Krzton-Maziopa, K. Conder, V. Pomjakushin, R. Pöttgen, and V. Dmitriev, Crystal structure of BaFe₂Se₃ as a function of temperature and pressure: phase transition phenomena and high-order expansion of landau potential, *J. Phys.: Condens. Matter* **25**, 315403 (2013).

[41] Y. Zhang, L.-F. Lin, J.-J. Zhang, E. Dagotto, and S. Dong, Sequential structural and antiferromagnetic transitions in BaFe₂Se₃ under pressure, *Phys. Rev. B* **97**, 045119 (2018).

[42] P. Kong, J. Wang, Y. Jin, C. Zhang, C. Lu, Y. Tian, and H. Chen, Exploration of high-pressure structural transition and electronic properties of BaFe₂S₃, *J. Phys.: Condens. Matter* **31**, 115401 (2019).

[43] V. Svitlyk, G. Garbarino, A. D. Rosa, E. Pomjakushina, A. Krzton-Maziopa, K. Conder, M. Nunez-Regueiro, and M. Mezouar, High-pressure polymorphism of BaFe_2Se_3 , *J. Phys.: Condens. Matter* **31**, 085401 (2019).

[44] S. Wu, J. Yin, T. Smart, A. Acharya, C. L. Bull, N. P. Funnell, T. R. Forrest, G. Simutis, R. Khasanov, S. K. Lewin, M. Wang, B. A. Frandsen, R. Jeanloz, and R. J. Birgeneau, Robust block magnetism in the spin ladder compound BaFe_2Se_3 under hydrostatic pressure, *Phys. Rev. B* **100**, 214511 (2019).

[45] W.-G. Zheng, V. Balédent, C. V. Colin, F. Damay, J.-P. Rueff, A. Forget, D. Colson, and P. Foury-Leykleian, Universal stripe order as a precursor of the superconducting phase in pressurized BaFe_2Se_3 spin ladder, *Commun. Phys.* **5**, 183 (2022).

[46] J. Ying, H. Lei, C. Petrovic, Y. Xiao, and V. V. Struzhkin, Interplay of magnetism and superconductivity in the compressed Fe-ladder compound BaFe_2Se_3 , *Phys. Rev. B* **95**, 241109 (2017).

[47] H. Sun, X. Li, Y. Zhou, J. Yu, B. A. Frandsen, S. Wu, Z. Xu, S. Jiang, Q. Huang, E. Bourret-Courchesne, L. Sun, J. W. Lynn, R. J. Birgeneau, and M. Wang, Non-superconducting electronic ground state in pressurized BaFe_2S_3 and $\text{BaFe}_2\text{S}_{2.5}\text{Se}_{0.5}$, *Phys. Rev. B* **101**, 205129 (2020).

[48] A. Krzton-Maziopa, E. Pomjakushina, V. Pomjakushin, D. Sheptyakov, D. Chernyshov, V. Svitlyk, and K. Conder, The synthesis, and crystal and magnetic structure of the iron selenide BaFe_2Se_3 with possible superconductivity at $T_c = 11$ K, *J. Phys.: Condens. Matter* **23**, 402201 (2011).

[49] J. M. Caron, J. R. Neilson, D. C. Miller, A. Llobet, and T. M. McQueen, Iron displacements and magnetoelastic coupling in the antiferromagnetic spin-ladder compound BaFe_2Se_3 , *Phys. Rev. B* **84**, 180409 (2011).

[50] M. Mourigal, S. Wu, M. B. Stone, J. R. Neilson, J. M. Caron, T. M. McQueen, and C. L. Broholm, Block magnetic excitations in the orbitally selective Mott insulator BaFe_2Se_3 , *Phys. Rev. Lett.* **115**, 047401 (2015).

[51] J. Rincón, A. Moreo, G. Alvarez, and E. Dagotto, Exotic magnetic order in the orbital-selective Mott regime of multiorbital systems, *Phys. Rev. Lett.* **112**, 106405 (2014).

[52] J. Herbrych, N. Kaushal, A. Nocera, G. Alvarez, A. Moreo, and E. Dagotto, Spin dynamics of the block orbital-selective Mott phase, *Nat. Commun.* **9**, 3736 (2018).

[53] M. Środa, E. Dagotto, and J. Herbrych, Quantum magnetism of iron-based ladders: Blocks, spirals, and spin flux, *Phys. Rev. B* **104**, 045128 (2021).

[54] J. M. Caron, J. R. Neilson, D. C. Miller, K. Arpino, A. Llobet, and T. M. McQueen, Orbital-selective magnetism in the spin-ladder iron selenides $\text{Ba}_{1-x}\text{K}_x\text{Fe}_2\text{Se}_3$, *Phys. Rev. B* **85**, 180405 (2012).

[55] N. D. Patel, A. Nocera, G. Alvarez, A. Moreo, S. Johnston, and E. Dagotto, Fingerprints of an orbital-selective Mott phase in the block magnetic state of BaFe_2Se_3 ladders, *Commun. Phys.* **2**, 64 (2019).

[56] H. Takahashi, A. Sugimoto, Y. Nambu, T. Yamauchi, Y. Hirata, T. Kawakami, M. Avdeev, K. Matsubayashi, F. Du, C. Kawashima, H. Soeda, S. Nakano, Y. Uwato, Y. Ueda, T. J. Sato, and K. Ohgushi, Pressure-induced superconductivity in the iron-based ladder material BaFe_2S_3 , *Nature Mater.* **14**, 1008 (2015).

[57] J. Gao, Y. Teng, W. Liu, S. Chen, W. Tong, M. Li, X. Zhao, and X. Liu, The synthesis and magnetic properties of BaFe_2Se_3 single crystals, *RSC Adv.* **7**, 30433 (2017).

[58] P. Materne, W. Bi, J. Zhao, M. Y. Hu, M. L. Amigó, S. Seiro, S. Aswartham, B. Büchner, and E. E. Alp, Band-width controlled insulator-metal transition in BaFe_2S_3 : A Mössbauer study under pressure, *Phys. Rev. B* **99**, 020505 (2019).

[59] S. Tewari and J. D. Sau, Topological invariants for spin-orbit coupled superconductor nanowires, *Phys. Rev. Lett.* **109**, 150408 (2012).

[60] P.-G. De Gennes, *Superconductivity of metals and alloys* (CRC press, 2018).

[61] A. V. Balatsky, I. Vekhter, and J.-X. Zhu, Impurity-induced states in conventional and unconventional superconductors, *Rev. Mod. Phys.* **78**, 373 (2006).

[62] A. Ptok, A. Kobiałka, and T. Domański, Controlling the bound states in a quantum-dot hybrid nanowire, *Phys. Rev. B* **96**, 195430 (2017).

[63] A. Cichy and A. Ptok, Superfluidity of fermionic pairs in a harmonic trap. comparative studies: Local density approximation and bogoliubov-de gennes solutions, *J. Phys. Commun.* **4**, 055006 (2020).

[64] K. Momma and F. Izumi, VESTA3 for three-dimensional visualization of crystal, volumetric and morphology data, *J. Appl. Crystallogr.* **44**, 1272 (2011).